Article

Ground Subsidence in the Beijing-Tianjin-Hebei Region from 1992 to 2014 Revealed by Multiple SAR Stacks

Yonghong Zhang [1],*, Hong'an Wu [1], Yonghui Kang [1] and Chuanguang Zhu [2]

[1] Chinese Academy of Surveying and Mapping, Beijing 100830, China; wuha@casm.ac.cn (H.W.);
     kangyh@casm.ac.cn (Y.K.)
[2] Hunan Province Key Laboratory of Coal Resources Clean-utilization and Mine Environment,
     Hunan University of Science and Technology, Changsha 411201, China; zhuchuanguang@163.com
*   Correspondence: yhzhang@casm.ac.cn; Tel.: +86-10-6388-0521

Abstract: The coordinated development of the Beijing-Tianjin-Hebei has become a national strategy with Beijing and Tianjin as twin engines driving the regional development. However, the Beijing-Tianjin-Hebei region has suffered dramatic ground subsidence during last two to three decades, mainly due to long-term groundwater withdrawal. Although, annual spirit leveling has been conducted routinely in some parts of Beijing and Tianjin, and InSAR technique has also been used to monitor ground subsidence in some local areas of the region, there is a lack of a complete survey of ground subsidence over the whole region. In this paper, we report a research on mapping ground subsidence in the Beijing-Tianjin-Hebei region over a long time span from 1992 to 2014. Three SAR datasets from four satellites are used: ERS-1/2 SAR images from 1992 to 2000, ENVISAT ASAR images from 2003 to 2010, and RADARSAT-2 images from 2012 to 2014. An improved multi-temporal InSAR method, namely "Multiple-master Coherent Target Small-Baseline InSAR" (MCTSB-InSAR), has been developed to process the datasets. A unique feature of MCTSB-InSAR is the adjustment process useful for wide area monitoring which provides an integrated solution for both calibration of InSAR-derived deformation and the harmonization of the deformation estimates from overlapping SAR frames. Three maps of the subsidence rate corresponding to the three periods over the wide Beijing-Tianjin-Hebei region are generated, with respective accuracy of 8.7 mm/year (1992–2000), 4.7 mm/year (2003–2010), and 5.4 mm/year (2012–2014) validated by more than 120 leveling measurements. The spatial-temporal characteristics of the development of ground subsidence in Beijing and Tianjin are analyzed. This research represents a first-ever effort on mapping ground subsidence over very large area and over long time span in China. The result is of significance to serve the decision-making on ground subsidence mitigation in the Beijing-Tianjin-Hebei region.

Keywords: multi-temporal Interferometric SAR; ground subsidence; Beijing-Tianjin-Hebei

1. Introduction

Beijing, the Capital of China, and Tianjin, one of the four municipalities of China, both play very important roles in the nation's political and economic framework. Especially since the coordinated development of Beijing-Tianjin-Hebei became a national strategy in 2013, in which Beijing and Tianjin are positioned as the twin engines driving the regional development. On the other side, due to insufficient rainfall in the North China plain, groundwater has been the main water resources for farmland irrigation, industrial activities, and daily water supply of urban inhabitants since 1970s [1]. Long-term over-withdrawal of groundwater has caused continuous and dramatic decline of groundwater level in the aquifer system of this region. For example, the groundwater level has

declined 2.7 m every year in Chaoyang district of Beijing from 2001 to 2010 [2]. Continuous pumping of aquifer water triggers large scale ground subsidence across the North China Plain. Currently, ground subsidence has been recognized as the most serious disaster hindering the sustainable development of this region. In 2012, the central government announced a 10-year plan (2012–2020 plan) swore to take measures fighting against ground subsidence in several main plains across the country including the North China Plain. Establishing an effective monitoring network over subsided areas was listed as a fundamental task of the plan.

Traditionally, the surveying and mapping agencies of Beijing and Tianjin have conducted spirit leveling once per year routinely since 1990s in some areas of Beijing and Tianjin. Therefore, ground subsidence information at some sparse leveling points has been obtained, which forms the basis of official reports on ground subsidence in Beijing and Tianjin. However, such a regular leveling campaign has never been conducted on a large scale in Hebei province, because the cost would be unaffordable given the area of more than 180,000 km^2 of Hebei province. The main drawback of the leveling method is that it cannot achieve dense spatial sampling due to cost limitations. For example, the area of Tianjin municipality is 11,946 km^2, while the amount of leveling points routinely measured every year is less than 1200, equivalent to about one leveling point within every 10 km^2. Therefore, ground subsidence information generated from leveling measurement is incomplete, thus having limited usefulness.

Interferometric SAR (InSAR) was considered an advantageous technique to monitor ground deformation over a large area in comparison with traditional ground-based methods when it emerged in late 1980s [3], but it did not become practically reliable until several kinds of advanced time series techniques came out around the end of last century, such as the permanent scatterer InSAR (PS-InSAR) [4–6] or persistent scattered InSAR [7], and the SBAS InSAR [8]. Since then, time series InSAR techniques have been widely applied to monitor various deformations across the geosciences community, including those associated with volcanic eruptions [9], earthquakes [10], landslides [11–13], and urban subsidence [14]. In China, given the significance of ground subsidence in the Beijing-Tianjin-Hebei region, time-series InSAR techniques have been employed to monitor ground subsidence in different cities, such as in Beijing [15–17], Tianjin [18–20], and Langfang [21] and Cangzhou [22] of Hebei province. All these studies concern subsidence over relatively small areas which can be covered by one SAR frame, and there is a lack of complete information on ground subsidence over the entire Beijing-Tianjin-Hebei region. In this paper, we report a research on monitoring ground subsidence using an improved time series InSAR technique for the wide Beijing-Tianjin-Hebei region over a 22-year time span dating back to 1992 when the European Remote Sensing (ERS)-1 SAR images became available. This research represents a first-ever effort on mapping ground subsidence over such a wide area in China. It involves not only technical innovations, but also significant output which can be used directly for decision-making on subsidence mitigation in the Beijing-Tianjin-Hebei region.

The paper is organized as follows. Section 2 describes the study area and the SAR images. The processing method is introduced in Section 3. The mosaics of ground subsidence rate during the three periods are presented in Section 4. The accuracy validation is also introduced in this section. In Section 5, the spatial-temporal characteristics revealed by the sequential subsidence rate over Beijing and Tianjin are described. Finally, conclusions and open problems are addressed in Section 6.

2. SAR Image Stacks and Study Area

We aim to investigate the ground subsidence of the Beijing-Tianjin-Hebei region for a period of 22 years. No single SAR system can provide images over such a long epoch. SAR images from four satellites are used: ERS-1/2 SAR images acquired between 1992 and 2000; Envisat ASAR images acquired between 2003 and 2010 and RADARSAT-2 images acquired between 2012 and 2014. Unfortunately, there are still three-year and two-year gaps between the sequential SAR datasets.

The plain area of the Beijing-Tianjin-Hebei region is targeted, because it has been confirmed that groundwater over-withdrawal is the main driving force of ground subsidence in this region and groundwater over-withdrawal mostly occurs in plain areas. Unfortunately, we could not obtain ERS and ENVISAT SAR images covering the south part of Hebei province. Therefore, for the period of 1992 to 2010, SAR images cover only the plain areas of Beijing, Tianjin, and Tangshan, Baoding and Langfang of Hebei province. For the period of 2012 to 2014, the whole plain area of the Beijing-Tianjin-Hebei region is covered by eight RADARSAT-2 wide mode frames. The study area and SAR coverages are shown in Figure 1. The number of SAR images over each SAR frame, together with the acquisition time span of the time series of images, are listed in Tables 1 and 2. We can see, the image stacks of ERS-1/2 are generally small, with the stack size less than 13 over 4 frames. The inadequacy causes difficulties in data processing and may result in less accurate deformation retrieval.
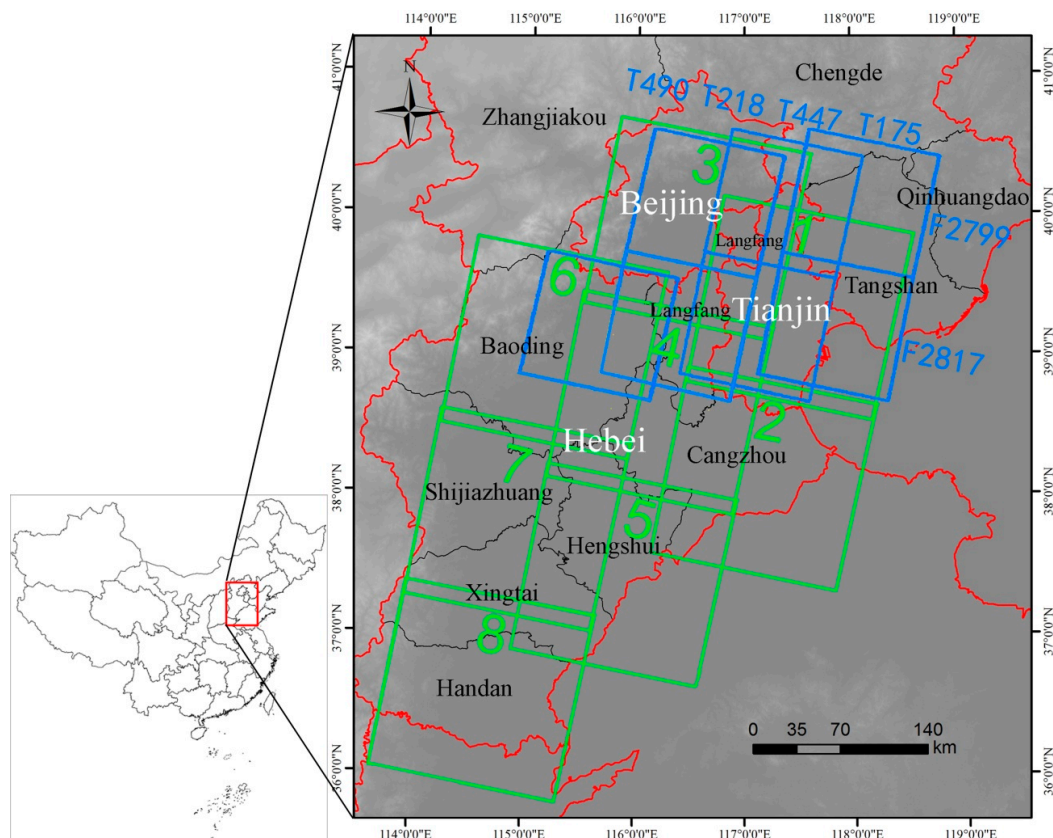

Figure 1. Location of the study area and coverage of SAR data for subsidence monitoring in the Beijing-Tianjin-Hebei region. A blue rectangle stands for the coverage of one ERS/ENVISAT SAR scene, and a green rectangle for one RADARSAT-2 SAR image. The background is SRTM DEM. The red lines denote provincial boundaries, and the black lines are municipal boundaries.

Table 1. Image numbers and acquisition time span of ERS-1/2 SAR and ENVISAT ASAR stacks.

Track/Frame	ERS-1/2 SAR Stacks		ENVISAT ASAR Stacks	
	Stack Size	Acquisition Time Span	Stack Size	Acquisition Time Span
218/2799	21	17 May 1992–9 June 2000	24	18 June 2003–29 September 2010
447/2799	12	11 August 1992–10 July 1998	21	18 June 2004–15 October 2010
175/2799	13	14 May 1992–21 May 2000	22	15 June 2003–26 September 2010
490/2817	12	18 September 1992–17 August 1998	17	5 August 2003–3 August 2010
218/2817	15	17 May 1992–2 September 1999	25	18 June 2003–29 September 2010
447/2817	10	28 April 1992–3 October 1997	24	17 October 2003–15 October 2010
175/2817	18	14 May 1992–25 June 2000	22	15 June 2003–26 September 2010

Table 2. Image numbers and acquisition time span of RADARSAT-2 stacks.

Frame No.	Stack Size	Acquisition Time Span
1	19	4 February 2012–11 July 2014
2	19	4 February 2012–11 July 2014
3	19	28 January 2012–4 July 2014
4	19	28 January 2012–4 July 2014
5	19	28 January 2012–4 July 2014
6	19	14 February 2012–27 June 2014
7	19	14 February 2012–27 June 2014
8	19	14 February 2012–27 June 2014

3. Methodology of Data Processing

An improved multiple InSAR method, which is entitled as "Multiple-master Coherent Target Small-Baseline InSAR" (MCTSB-InSAR), is developed to process time-series SAR images over a large area. The basic algorithms of MCTSB-InSAR are based on some classical multiple InSAR methods, like PS-InSAR [5,6], that presented in [23] and the PSP method in [24]. The general processing flowchart for deformation mapping over large area using the MCTSB-InSAR method is shown in Figure 2. When dealing with large area consisting of several SAR frames, the deformation over a single SAR frame is estimated first. Then, an adjustment process is employed to harmonize the deformation of overlapping frames, so that a deformation mosaic of the whole area can be generated. The adjustment process will be described in detail later. Some key steps of the method are overviewed in the paragraphs followed.

In the step of interferogram formation, interferograms with spatial baseline and temporal separation within specified thresholds are selected, not limited to one common master image. This is helpful when dealing with small dataset, like the ERS-1/2 stacks over those four frames in this research. The coherent targets include two kinds of pixels. The first type is those pixels characterized by point scatterers whose amplitude keeps stable over temporal acquisitions. These pixels are extracted by thresholding the dispersion index defined by Ferretti et al. [6]. The other type is those pixels associated with stable distributed targets which can be extracted by checking the mean coherence of the formed interferograms [23]. These two groups of pixels are then united and form the coherent target candidates over which the rest processing is conducted.

Similar with the PS-InSAR and the PSP method [24], the phase difference between two neighboring coherent targets are considered in MCTSB-InSAR. Therefore the coherent targets have to be networked firstly. The Delaunay triangulation has been widely employed in many multiple InSAR processing. However, the network generated by Delaunay triangulation is not robust [25]. MCTSB-InSAR adopts the local Delaunay triangulation proposed by Zhang et al. [26] which places small overlapping and regular patches over the entire study area, and then connects the coherent targets within each patch using Delaunay triangulation. The local Delaunay triangulation performs well in balancing the robustness and redundancy of connections. The final density of the arcs generated by local Delaunay triangulation can be controlled by setting the size of the patch and the overlapping rate of two adjoining patches. Figure 3 shows the performance of networking with Delaunay triangulation and with local Delaunay triangulation over an image subset consisting of 640 pixels in a row (about 12.8 km) and 600 pixels in a column (about 12.0 km) and 3363 coherent targets. The number of arcs generated by Delaunay triangulation is 9959, sparser than any of the three connections from local Delaunay triangulation. Generally, we will obtain dense connections if the patch size is small and the overlapping rate is high. Of course, to keep atmospheric phase cancelable along an arc, only arcs shorter than a threshold (1.2 km in this research) are kept.
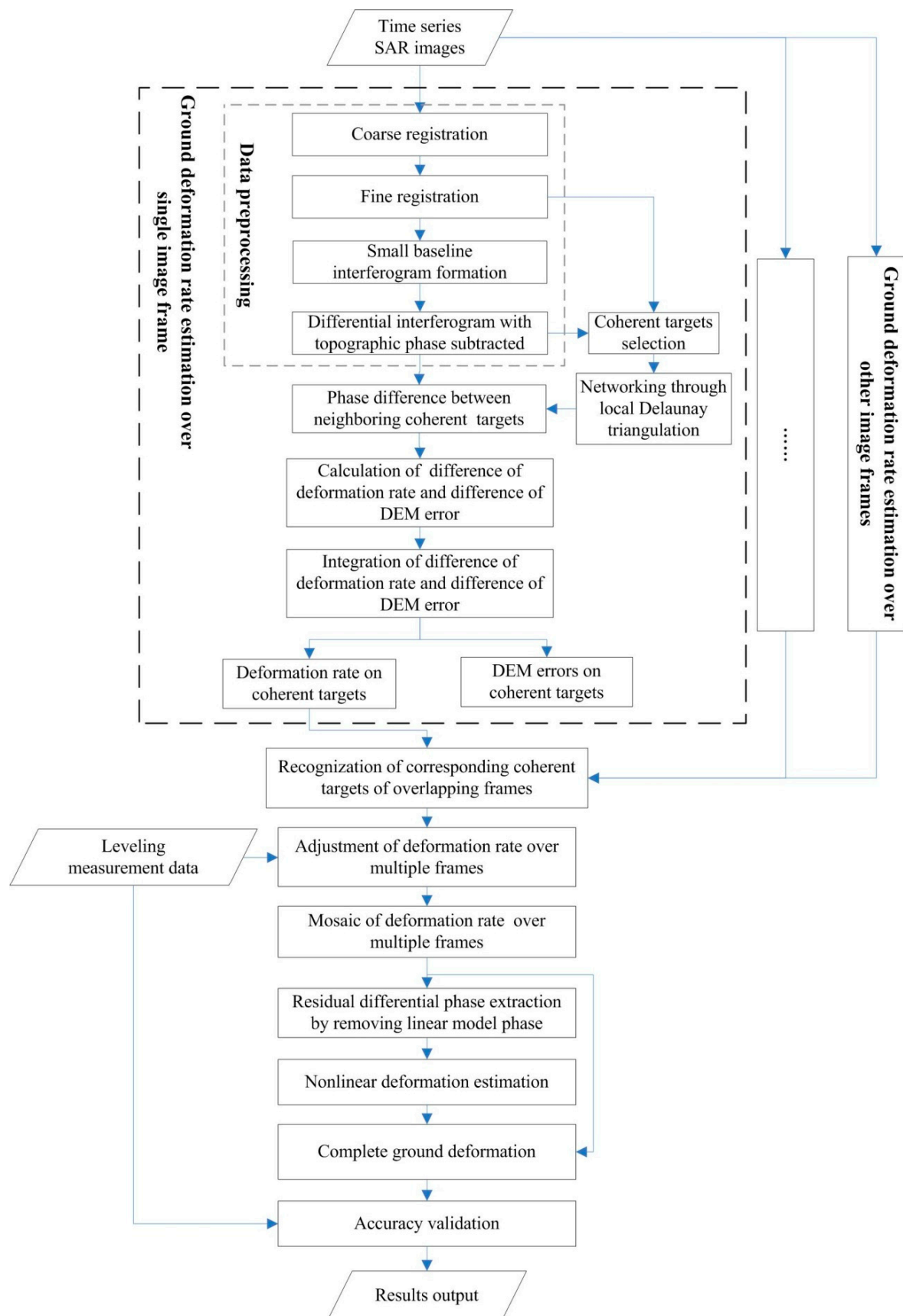
Figure 2. Processing flow chart of mapping ground deformation over large area using the MCTSB-InSAR method.
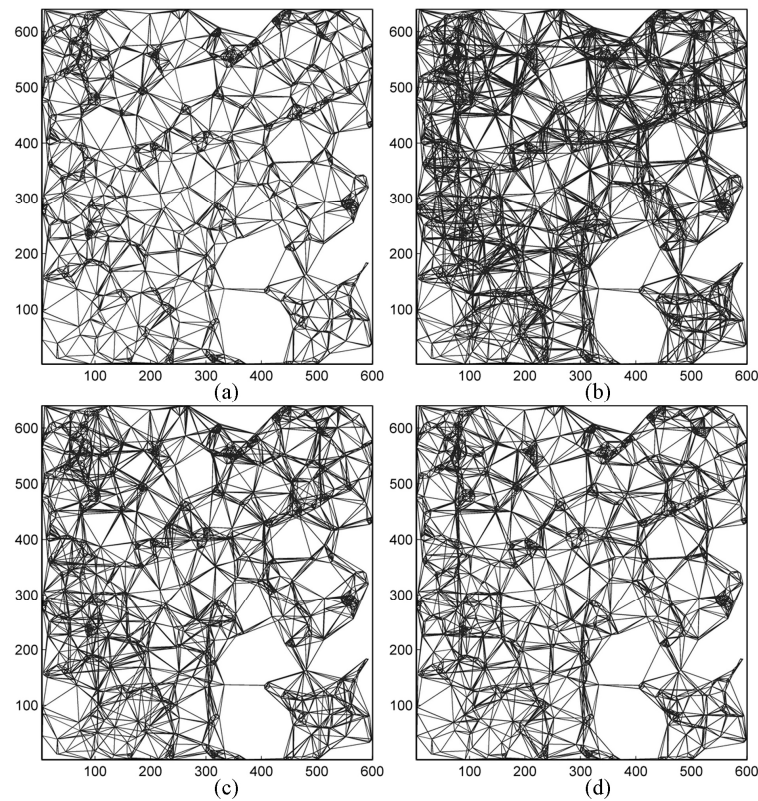
Figure 3. Comparison of networking with Delaunay triangulation and local Delaunay triangulation. (**a**) is the network from Delaunay triangulation, which has 9959 arcs; (**b**) is from local Delaunay triangulation with patch size of 100 × 100 pixels and overlapping rate of 75%, and has 13,306 arcs; (**c**) is from local Delaunay triangulation with patch size of 100 × 100 pixels and overlapping rate of 50%, and has 11,575 arcs; (**d**) is from local Delaunay triangulation with patch size of 150 × 150 pixels and overlapping rate of 50%, and has 11,104 arcs.

Currently, the linear deformation model is used in MCTSB-InSAR for large area monitoring, that is, the main part of deformation is represented by a linear process with fixed rate, and the residual deformation is expressed as a non-linear process. More complicated deformation models such as high-order polynomial might be applicable for small region, but will cause problems in generating a mosaic of derived deformation for a large area consisting of several SAR frames. Under linear deformation assumption, the interferometric phase of the *i*th coherent target in the *k*th interferogram (The interferogram here is a differential interferogram with topographic phase having been subtracted using a DEM) is

$$\varphi_i^k = wrap\{a_1 B_{i,\perp}^k \cdot \Delta h_i + a_2 t_i^k \cdot v_i + \varphi_{i,non-linear}^k + \varphi_{i,atmo}^k + \varphi_{i,noise}^k\} \tag{1}$$

where $wrap\{\}$ denotes phase wrapping operator, $B_{i,\perp}^k$ and t_i^k are the perpendicular baseline and the temporal separation of the interferogram respectively, Δh_i is the DEM error, v_i is the linear deformation rate, $\varphi_{i,non-linear}^k$ is the phase associated with non-linear deformation, $\varphi_{i,atmo}^k$ is the phase caused by atmospheric artifacts, and $\varphi_{i,noise}^k$ the phase accounting for noise, a_1 and a_2 are known coefficients. Consequently, the phase difference between two neighboring coherent targets along an arc can be expressed as

$$\Delta \varphi_{i,j}^k = wrap\{a_1 B_{i,\perp}^k \cdot \Delta h_{i,j} + a_2 t^k \cdot \Delta v_{i,j} + \Delta \varphi_{i,j,res}^k\} \tag{2}$$

where $\Delta h_{i,j}$ and $\Delta v_{i,j}$ denote the difference of deformation rate and difference of DEM error between the two targets *i* and *j*, the residual phase $\Delta \varphi_{i,j,res}^k$ is the summation of atmospheric phase difference,

noise phase difference and non-linear phase difference over the two targets. For each arc, we will form a set of equations like (2) with each corresponding to an interferogram. The unknown variables of the equation set, namely $\Delta h_{i,j}$ and $\Delta v_{i,j}$, can be solved using the periodogram [5] or 2-D searching algorithm [27]. After all arcs in the network are processed, the absolute values of the linear deformation rate v and DEM error Δh for each coherent target can be calculated through an integration process.

After the deformation rate over every single SAR frame has been estimated, an adjustment process is employed to harmonize the deformation estimates from overlapping frames, which is a unique feature of the MCTSB-InSAR method, and has seldom been discussed by other multiple InSAR methods yet. Here only the adjustment of deformation rate is concerned. Accumulative deformations are difficult to be mosaicked, because the time span of SAR images over different tracks are usually different. Before the adjustment, the corresponding coherent targets from overlapping frames have to be recognized. This can be done easily on the basis of geocoded images. The underlying principle is that the geographic coordinates of two corresponding coherent targets should be similar, that is, the difference of their coordinates should be smaller than the grid size of geocoding. The adjustment is to estimate an offset adding to the calculated deformation rate for a frame, so that the adjusted deformation rate over corresponding coherent targets within overlapped area of neighboring frames is identical. This forms the first category of adjustment equations, which has the following form

$$v_L(x, y) + \Delta L = v_R(x, y) + \Delta R \tag{3}$$

where v_L and v_R are InSAR-derived deformation rate over a corresponding coherence target at position (x, y) from overlapped frame L and R, ΔL and ΔR are the unknown offset of deformation rate. On the other hand, the deformation rate calculated from leveling and/or GPS measurements can be used as reference of the adjustment. Especially, the adjusted deformation rate should be equal to that calculated from the reference data, which forms the second category of adjustment equations and has the following form

$$v_L(x, y) + \Delta L = v_{ref}(x, y) \tag{4}$$

where $v_{ref}(x, y)$ denotes deformation rate calculated from leveling and/or GPS measurements. The two groups of equations join together and form an over-determined linear system with the offset attached to every overlapped frame as unknown variables. Obviously, these unknowns can be solved under the least mean square criterion. Finally, a deformation rate mosaic is formed by averaging the adjusted deformation rates of overlapping frames. The adjustment process is powerful in large area monitoring. It provides an integrated solution for both calibration of InSAR-derived deformation rate for every frame and the harmonization of the deformation rates from overlapping frames.

Once the linear deformation rate is determined, the nonlinear deformation is estimated by temporal and spatial filtering of the residual phase. More information about nonlinear deformation estimation can be found in [5,23].

4. Result and Accuracy

The three sets of SAR stacks are processed and the deformation of the study area over the three time spans is calculated, respectively. ERS-1/2 and ENVISAT SAR images are multilooked with a pixel size on the ground of 40 m. RADARSAT-2 images are multilooked, with a pixel size of 25 m on the ground. The numbers of final coherent targets over the study area are 518,150 in ERS-1/2 images, 982,045 in ENVISAT images, and 4,906,691 in RADARSAT-2 images. The deformation rate mosaic of the three time spans is shown in Figures 4–6, respectively. Please note the deformation rate in SAR line-of-sight (LOS) direction has been projected into the up-down direction as subsidence rate according to Equation (5):

$$v_{u-d}(x, y) = v_{LOS}(x, y) / \cos\theta_{(x,y)} \tag{5}$$

where, $v_{u-d}(x, y)$ and $v_{LOS}(x, y)$ are the up-down subsidence rate and SAR LOS deformation rate respectively, $\theta_{(x,y)}$ is SAR viewing angle at position (x, y). Of course, Equation (5) holds only under an ideal condition that ground uplift or subsidence is the sole deformation. For this study, this assumption is reasonable, because it has been widely recognized that ground subsidence and uplift are the dominant ground deformations in the North China plain [1]. Another reason for doing so is to facilitate the generation of the subsidence rate mosaic for the wide Beijing-Tianjin-Hebei region. The study area is covered by SAR images from at least three tracks, and the SAR LOS varies with different tracks. Therefore, in order to generate a mosaic of the deformation rate, we have to choose a SAR LOS as the reference direction, and project the deformation rate of other LOS into this direction. This process also involves some assumptions. In conclusion, projecting the deformation rate of all SAR LOSs into the up-down direction may be a good solution. In the figures, positive value means uplift, and negative value means subsidence. We have to admit that the subsidence rate estimated from ERS-1/2 SAR stacks over some frames is not very accurate, which cause obvious inconsistency between neighboring frames, like the frame 2817 and 2799 of track 175 as shown in Figure 4. Also from Figure 4, there are some noisy points showing uplift at the rate of 6–15 mm/year, which is inconsistent with the neighboring subsidence. As mentioned in Section 2, the relatively small size of the image stack and the heterogeneous spatial and temporal baseline of ERS-1/2 images may result in a less accurate deformation estimate, thus producing inconsistency in the mosaic. In contrast, the subsidence rate mosaic generated from ENVISAT and RADARSAT-2 dataset shows very good consistency, which indirectly indicates that the deformation rate estimates are accurate. You may notice there are obvious uplifts in the south-western mountainous areas in Figure 6. This may be caused by some topography induced atmospheric artifacts, or real ground uplift. Unfortunately, there is no leveling measurements over there. Further research is needed to investigate the uplift over the mountainous areas.
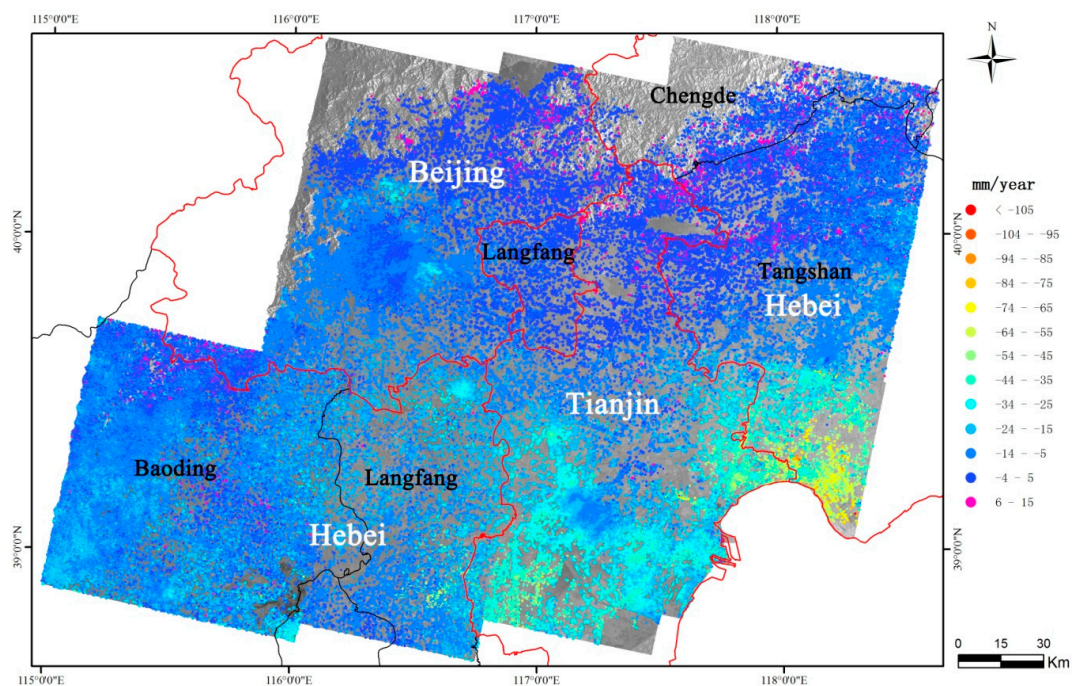

Figure 4. Linear subsidence rate over the Beijing-Tianjin-Hebei region from 1992 to 2000 observed by time series ERS-1/2 SAR images. The red lines denote provincial boundaries, and the black lines are municipal boundaries.
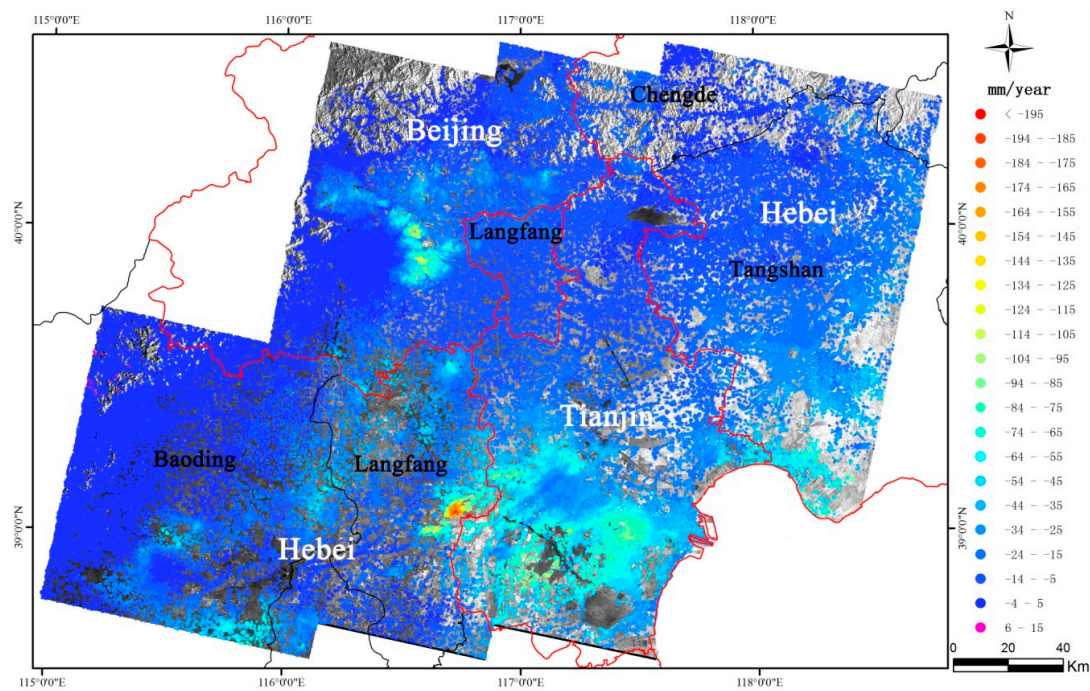
Figure 5. Linear subsidence rate over the Beijing-Tianjin-Hebei region from 2003 to 2010 observed by time series ENVISAT ASAR images.
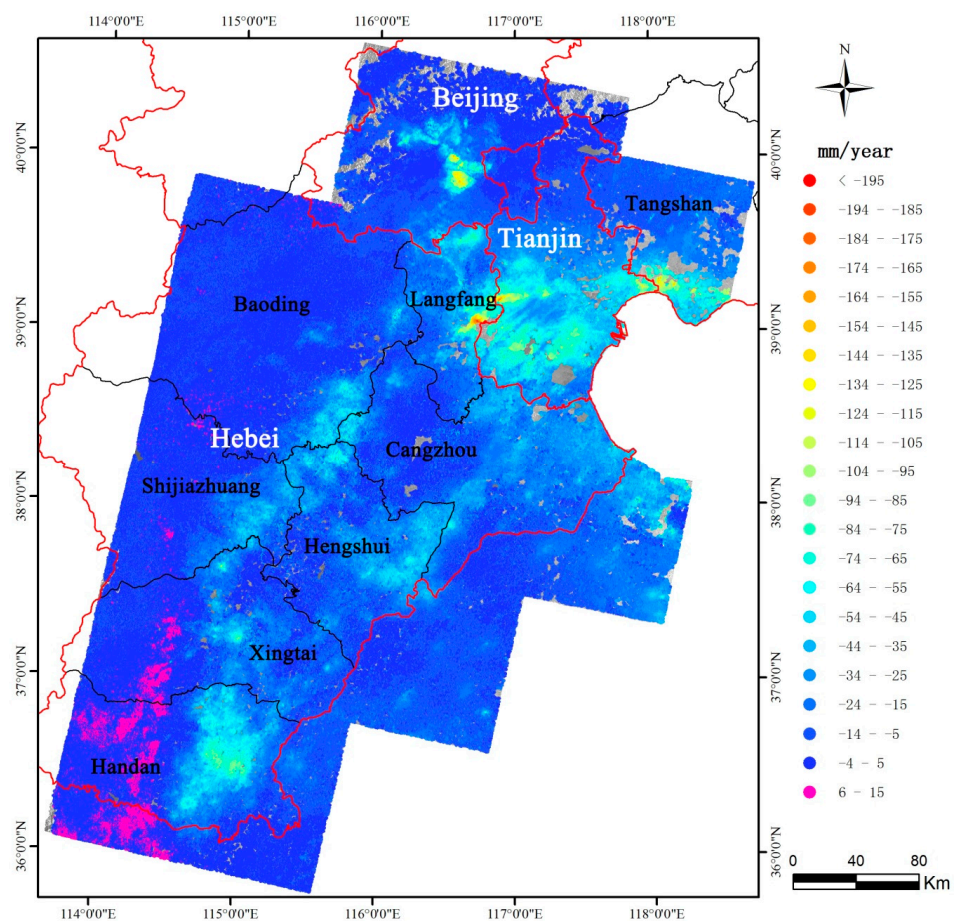

Figure 6. Linear subsidence rate over the Beijing-Tianjin-Hebei region from 2012 to 2014 observed by time series RADARSAT-2 images.

We have collected subsidence measurements over 204 leveling points from the surveying and mapping authority of Tianjin, which were measured every October from 1992 to 2014, and subsidence measurements over 169 leveling points measured annually through 2005 to 2012, and 34 leveling points measured annually through 2012 to 2014 from the surveying and mapping authority of Beijing. Of course, not all of these leveling points are usable, because there may not be a coherent InSAR target in the vicinity of a leveling point. Only those leveling points in a circle neighborhood with 80-m radius centered where there is at least one coherent target are used. Generally, around one third of those usable leveling measurements are used as reference in the adjustment process, and the rest are used to evaluate the accuracy of InSAR-derived subsidence rate. For example, totally 211 leveling points are used in the processing of RADARSAT-2 dataset. Out of them, 70 points are used as the references of adjustment, and 141 points are used in accuracy evaluation. The locations of the 211 leveling points are plotted in Figure 7a, where the blue points are for adjustment reference, and the red points for accuracy evaluation. The statistics of the evaluation result are listed in Table 3, including the standard deviation of the difference between subsidence rate derived from InSAR and leveling measurement, and the maximum and minimum values of the difference. The differences between the subsidence rate derived from RADARSAT-2 dataset and that from leveling measurement over the 141 red points in Figure 7a are shown in Figure 7b. The standard deviation in Table 3 indicates that the subsidence rate derived from ASAR and RADARSAT-2 images have an accuracy of 4.7 mm/year and 5 mm/year respectively, while the subsidence rate derived from ERS-1/2 images has an accuracy of 8.7 mm/year, not as good as the other two. Of course, the leveling measurements are back-projected into the SAR LOS direction in the accuracy evaluation in some publications. From Equation (5), it can be seen that the evaluation result of these two processes is linearly correlated. In this case, you may obtain an little better accuracy result if the leveling measurements are back-projected into SAR LOS, as the scaling factor $\cos\theta_{(x,y)}$ tends to reduce the values of deformation. The evaluation results in Table 3 agree with the visual quality of the three mosaics of subsidence rate shown in Figures 4–6. This also confirms that the deformation rate derived from the three SAR dataset is generally accurate and the MCTSB-InSAR method is reliable.

Table 3. Statistics of accuracy evaluation of InSAR-derived subsidence rate in three periods (mm/year).

Time Spans	Number of Used Leveling Points	Maximum Difference	Minimum Difference	Standard Deviation of Difference
1992–2000	123	14	−12	8.7
2003–2010	166	11	−14	4.7
2012–2014	141	11	−16	5.4

Besides the subsidence rate, the accumulative subsidence over individual coherent targets can also be estimated from one SAR stack. As mentioned earlier, there are two-to-three year gaps between the three sequential SAR stacks, therefore we can only obtain three discrete time series of accumulative subsidence for the period of 1992 to 2014. However, by means of the continuous annual leveling measurements over some parts of the region, such as Tianjin, the three discrete time series of accumulative subsidence can be linked together to form a continuous time series of ground subsidence. Figure 8 shows the time series of subsidence over four coherent targets in Tianjin, together with the subsidence series from the nearest leveling point. The positions of the four coherent targets are marked in Figure 7b. We can see that the time series of InSAR-derived subsidence fit well with the subsidence evolution recorded by leveling measurements, which conforms the accuracy of the ground subsidence mapped by InSAR.
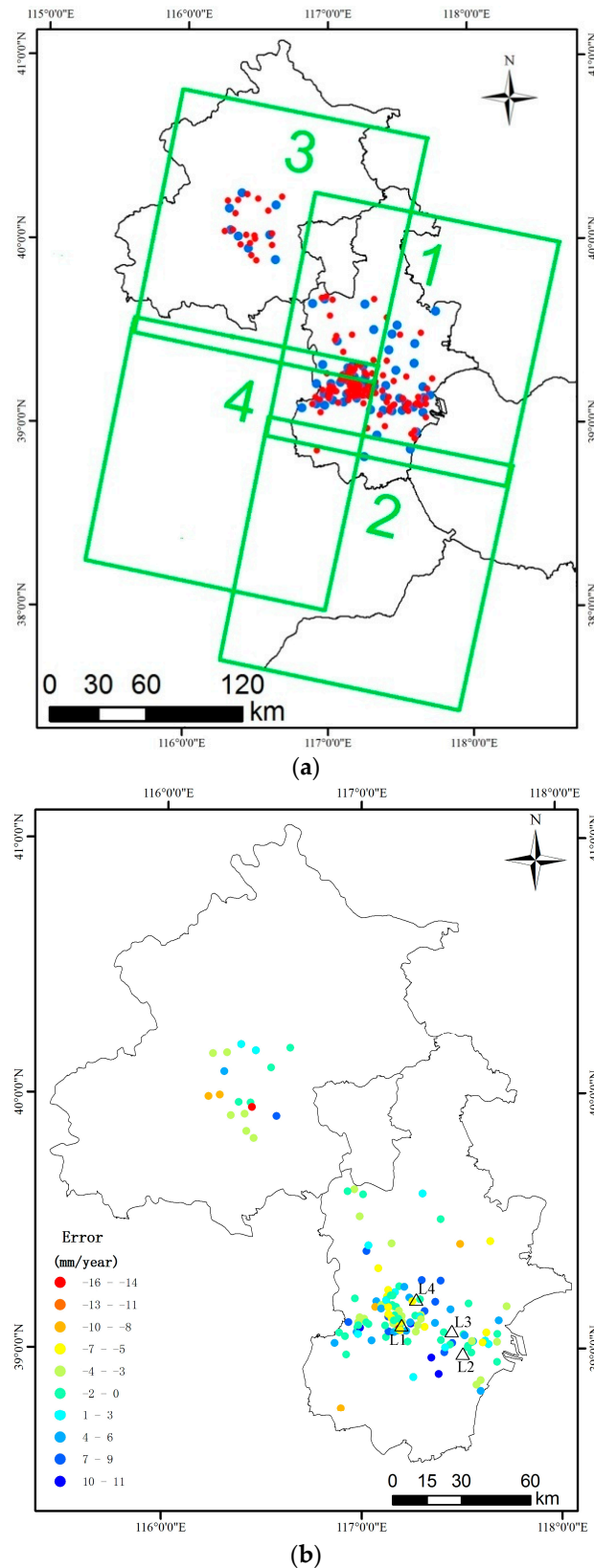
(**a**)

(**b**)

Figure 7. Locations of the 211 leveling points used for adjustment reference and accuracy evaluation of the subsidence rate generated from the RADARSAT-2 dataset (**a**); Blue points are for adjustment reference, and red points for accuracy evaluation. The errors of InSAR derived subsidence rate over the 141 red points are shown in (**b**). The four triangles in (**b**) mark the locations of the four coherent targets whose subsidence evolution is shown in Figure 8.
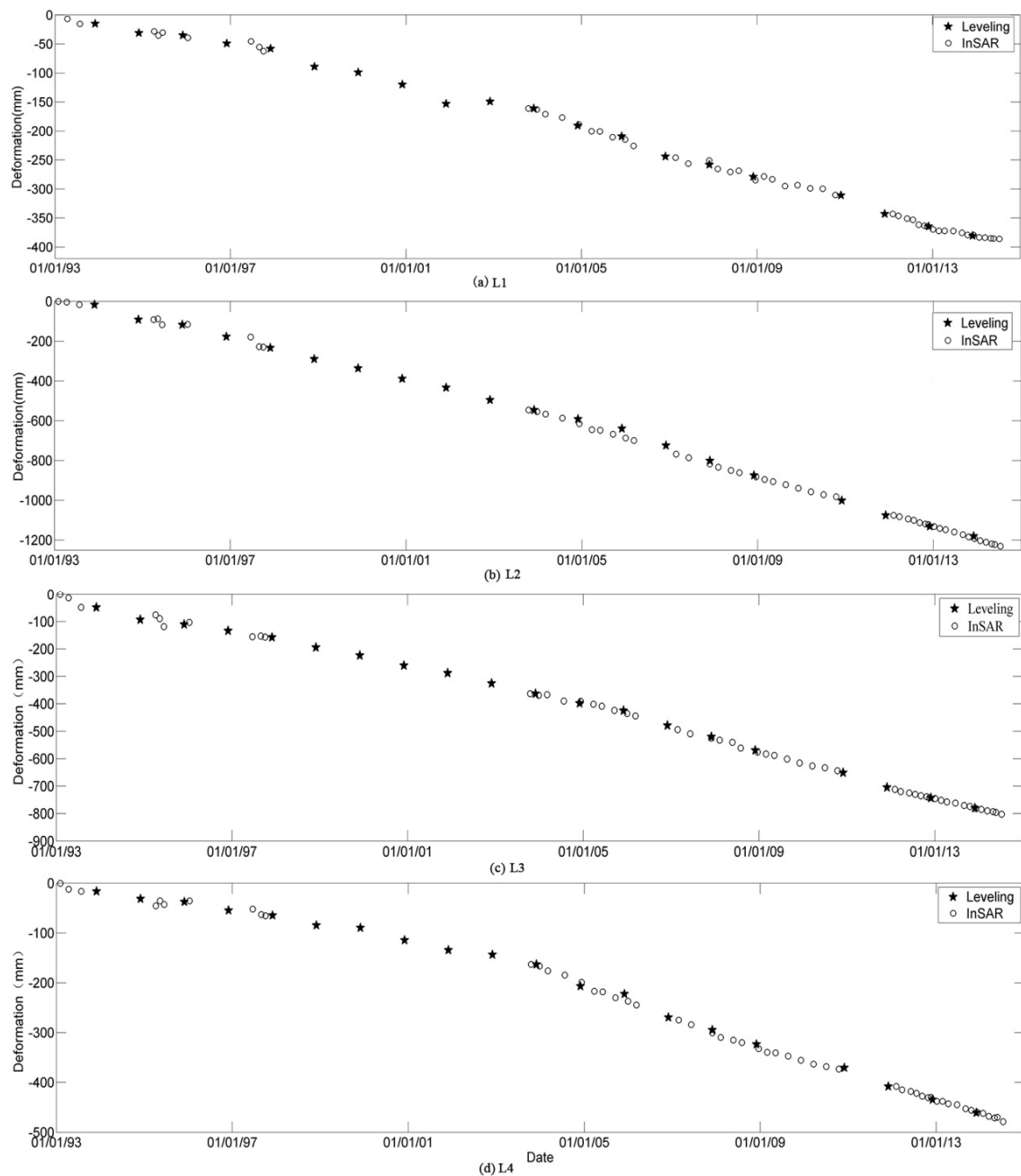
Figure 8. (**a–d**) The time series of accumulative subsidence over four coherent targets in Tianjin, together with the subsidence series of the nearby leveling point.

5. Spatial—Temporal Variation of Ground Subsidence in Beijing and Tianjin

The subsidence rate of the Beijing plain area over the three time spans is shown in Figure 9. During the time span from 1992 to 2000, most of the Beijing plain is stable. Some small scale subsidence took place in Haidian, Changping, Chaoyang, and Mentougou districts. The maximum subsidence rate is 48 mm/year in this period which occurred at a mining site in Mentougou district marked by the redline circle in Figure 9b. The coal exploited in this mine had been the main energy source for heating Beijing during the winter for decades. The mine site was shut down in 2000. From Figure 9c, the previous subsiding sites in the Chaoyang district had evolved as large subsiding zones, with a maximum rate reaching 143 mm/year. Subsiding zones also existed in the north part of the Beijing plain, including Haidian, Changping, Shunyi, and Pinggu districts. To count the subsiding area, the subsidence rate

over non-coherent pixels is estimated using the simple Kriging interpolation method with the normal score transformation and spherical semivariogram model in ArcGIS software. Totally, the subsiding area with a subsidence rate of more than 50 mm/year was 265.41 km^2. A noticeable change is that the subsidence at the mining site in the Mentougou district disappeared, which turned out to be the result of the shutdown. During the period from 2012 to 2014 as shown in Figure 9d, the subsidence in the Beijing plain had continuously developed, with 433.25 km^2 area subsiding at a rate more than 50 mm/year. The subsiding zones of Chaoyang, Tongzhou, Haidian, Changping, and Shunyi districts kept growing and became geographically joined together. The maximum subsidence rate was 152 mm/year, even higher than that of the previous time span. Generally, during the last two decades, ground subsidence mainly occurred in the east and north part of the Beijing plain, with the east rim of Chaoyang district and the northwest part of Tongzhou district suffering the most severe subsidence. The urban center consisting of Xicheng and Dongcheng districts and the western part of Beijing kept relatively stable with little subsidence. More analysis on the relationship between the temporal-spatial variations of ground subsidence and the groundwater exploration and the hydro-geological environment in Beijing is needed in the future.
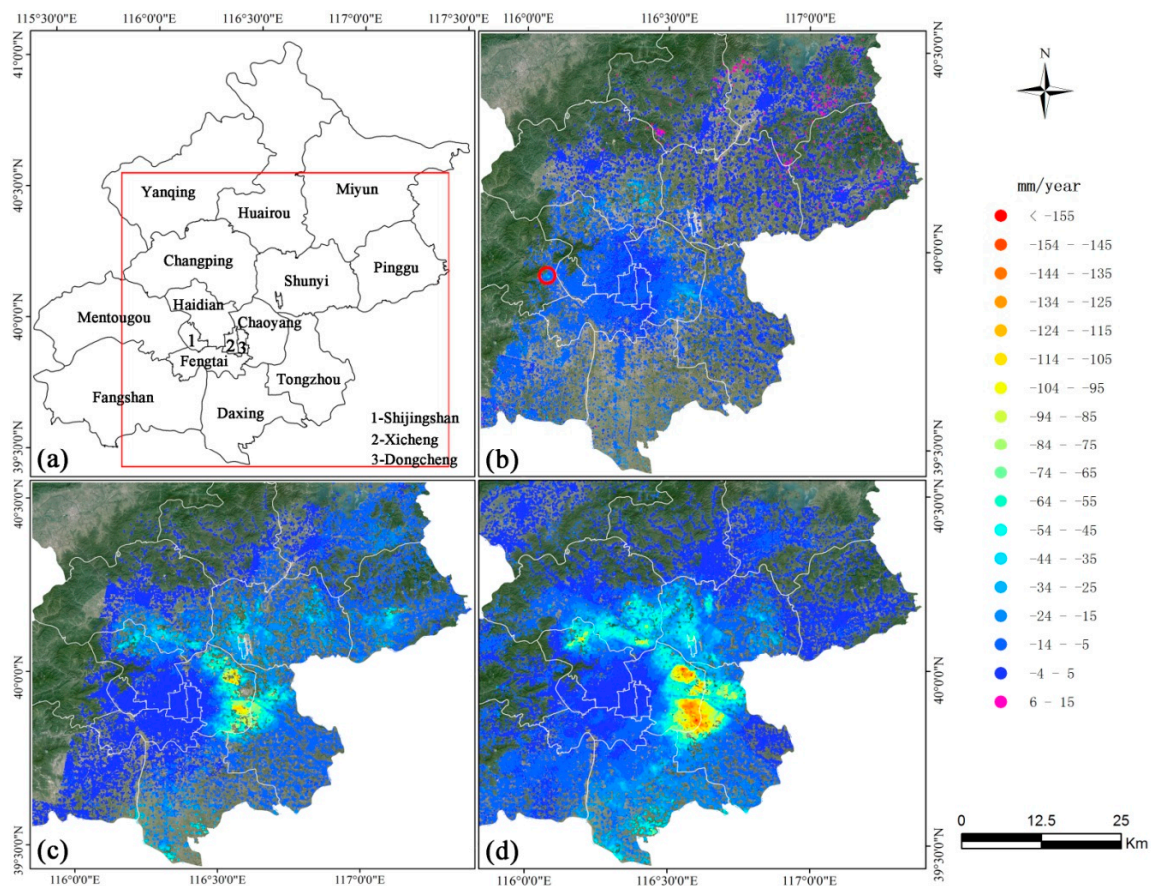

Figure 9. (**a**–**d**) Subsidence rate in three stages in Beijing. (**b**) 1992–2000; (**c**) 2003–2010; (**d**) 2012–2014. The districts and counties of Beijing municipality are shown as polygons in (**a**) with their names embedded. The redline rectangle in (**a**) corresponds to the area shown in (**b**–**d**). A mining site in Mentougou district marked by the redline cycle in (**b**) had the largest subsidence rate from 1992 to 2000.

The spatial-temporal characteristic of subsidence in Tianjin is a little different from that of Beijing. The maps of subsidence rate of Tianjin in the three time spans are shown in Figure 10. During the time span from 1992 to 2000, ground subsidence took place in nearly all the suburb districts surrounding the urban center, including Wuqing, Beichen, Xiqing, Jinghai, Dongli, Jinnan, Tanggu, and Hangu districts. The majority of the subsidence rate was in the range of 30 mm/year to 60 mm/year. The maximum subsidence rate was 81 mm/year. The area with a subsidence rate more than 50 mm/year was

85.73 km^2, in comparison to none in Beijing at that period. During the period from 2003 to 2010, ground subsidence had developed very quickly. In the north, west, and south of the urban center, ground subsidence had expanded dramatically, especially in districts of Beichen, Xiqing, Jinghai, Dongli, and Jinnan as shown in Figure 10c. Only in the coastal area of Hangu district was ground subsidence relieved somehow. The maximum subsidence rate of Tianjin at this period reached 135 mm/year. The area with a subsiding rate more than 50 mm/year was 2749.1 km^2, 10 times of that in Beijing. During the period from 2012 to 2014, ground subsidence in Tianjin presented different scenario over the north part and south part which was approximately marked by the white solid line in Figure 10c,d. In the northern part, ground subsidence was exacerbated, especially in districts of Beichen and Wuqing. The subsided area became wider, and the subsidence rate became larger. The largest subsidence occurred at the town of Wangqingtuo of the Wuqing district reaching 153 mm/year. In the south part of Tianjin, ground subsidence showed substantial alleviation, which might be the result of control of groundwater exploration in recent years in this region. As a comparison, the area with a subsiding rate more than 50 mm/year decreased to 1117.55 km^2 in the period of 2012 to 2014, roughly 41% of the area in previous period. In summary, ground subsidence in Tianjin had already been serious in 1990s, had dramatically expanded during 2000s, and started to alleviate in recent years.
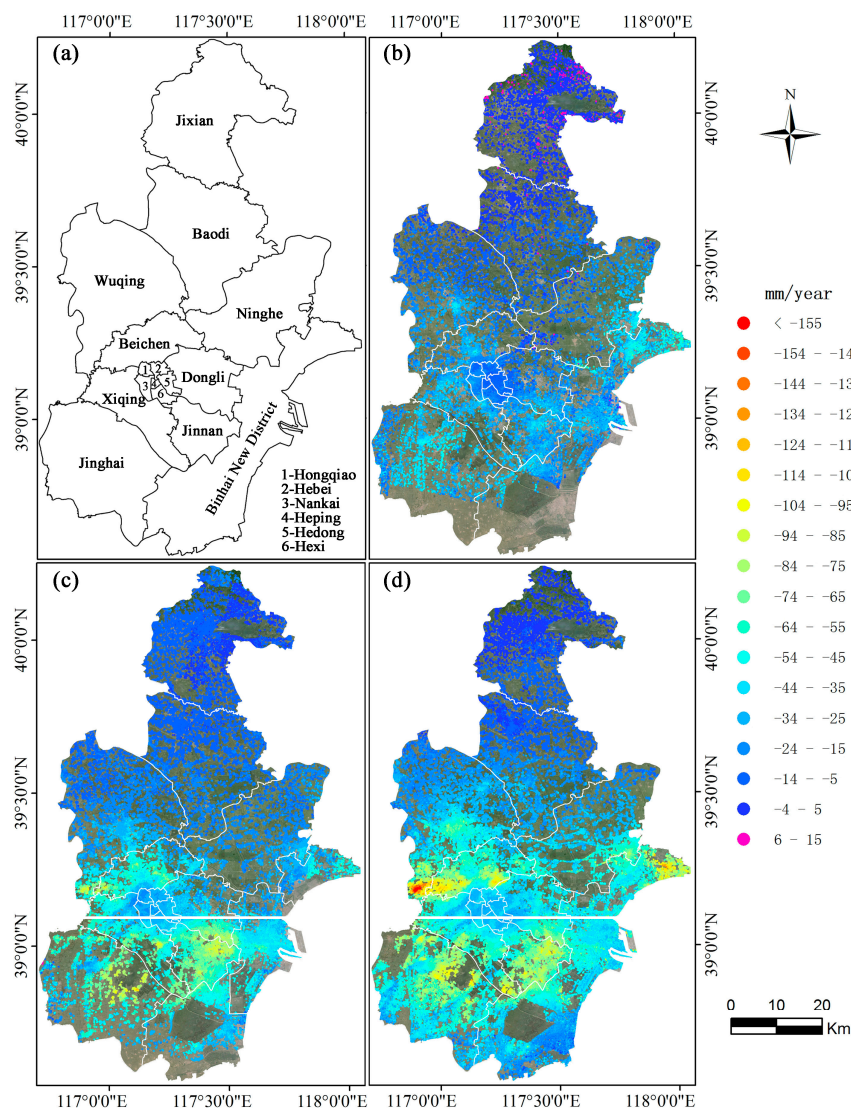

Figure 10. (**a**–**d**) Subsidence rate in the three periods in Tianjin; (**b**) 1992–2000; (**c**) 2003–2010; (**d**) 2012–2014. The districts and counties of Tianjin municipality are shown as polygons in (**a**) with the names on.

6. Conclusions

An application using multi-temporal InSAR technology to map ground subsidence over the wide Beijing-Tianjin-Hebei region is presented. Three sets of SAR images coming from four satellites are employed to cover a long time span from 1992 to 2014. An improved time series InSAR methodology, namely MCTSB-InSAR, has been developed to deal with small datasets consisting of only 11 to 12 images and to monitor deformation over wide area equivalent to the coverage of several SAR frames. The adjustment process of MCTSB-InSAR provides an integrated solution for both calibration of InSAR-derived deformation and the harmonization of the deformation estimates from overlapping frames. Of course, some aspects of MCTSB-InSAR need to be improved further. For example, the currently used linear deformation model may not fit a situation with strong non-linear deformation. More complicated deformation models, such as high-order polynomial and sinusoid model as presented in [28] should be incorporated into MCTSB-InSAR in the future.

Three subsidence rate maps over the Beijing-Tianjin-Hebei region on three time spans are generated from SAR images acquired by ERS-1/2, ENVISAT, and RADARSAT-2 satellites. Compared with more than 120 leveling measurements collected in Beijing and Tianjin, the subsidence rate maps have a standard deviation of 8.7 mm/year (1992–2000), 4.7 mm/year (2003–2010), and 5.4 mm/year (2012–2014) respectively. The comparison validates the accuracy the subsidence information derived from InSAR, and confirms the reliability and robustness of the MCTSB-InSAR method.

During the 22-year time span, the evolution of ground subsidence in Beijing and Tianjin shows different scenarios. In the period from 1992 to 2000, there were only some sites with small-scale subsidence mainly scattered in the eastern and northern suburbs of Beijing, with the largest rate being 48 mm/year; while in Tianjin, serious ground subsidence already took place in nearly all the suburb districts with 85.73 km^2 area subsiding at a rate more than 50 mm/year. In the period of 2003 to 2010, ground subsidence had expanded dramatically in both Beijing and Tianjin. In the period of 2012 to 2014, ground subsidence in Beijing had continuously developed, with the area subsiding at a rate more than 50 mm/year increasing 63% than that of the previous period; while the development of ground subsidence in Tianjin had slowed down with the area subsiding at a rate more than 50 mm/year decreasing 41% than that of the previous period. The different spatial-temporal characteristics of subsidence evolution in Beijing and Tianjin surely were related to the exploration of groundwater, precipitation, hydro-geological environment, and others. How these factors affected ground subsidence need further analysis in the future.

The output of the research provides first-hand, relatively complete and accurate information about ground subsidence over the Beijing-Tianjin-Hebei region. This information could directly serve the decision-making on ground subsidence mitigation and water resource management in the Beijing-Tianjin-Hebei region.

Author Contributions: Yonghong Zhang led this research, designed the framework of data processing, and developed the adjustment algorithm. Hong'an Wu contributed to algorithm programming, the Radarsat-2 data processing and accuracy evaluation. Yonghui Kang processed the ERS-1/2 SAR data and contributed to accuracy evaluation. Chuanguang Zhu contributed to the ENVISAT ASAR data processing.

Conflicts of Interest: The authors declare no conflict of interest.

References

1. He, Q.C.; Liu, W.B.; Li, Z.M. Land subsidence survey and monitoring in the North China plain. *Geol. J. China Univ.* **2006**, *12*, 195–209. (In Chinese)
2. Yang, Y.; Jia, S.M.; Wang, H.G. The status and development of land subsidence in Beijing plain. *Shanghai Geol.* **2010**, *31*, 23–28. (In Chinese)

3.　Gabriel, A.K.; Goldstein, R.M.; Zebker, H.A. Mapping small elevation changes over large areas: Differential radar interferometry. *J. Geophys. Res. Atmos.* **1989**, *94*, 9183–9191. [CrossRef]

4.　Ferretti, A.; Prati, C.; Rocca, F. Permanent scatterers in SAR interferometry. In Proceedings of the IEEE International Geoscience and Remote Sensing Symposium, Hamburg, Germany, 28 June–2 July 1999; pp. 1528–1530.

5.　Ferretti, A.; Prati, C.; Rocca, F. Nonlinear subsidence rate estimation using permanent scatterers in differential SAR interferometry. *IEEE Trans. Geosci. Remote Sens.* **2000**, *38*, 2202–2212. [CrossRef]

6.　Ferretti, A.; Prati, C.; Rocca, F. Permanent scatterers in SAR interferometry. *IEEE Trans. Geosci. Remote Sens.* **2001**, *39*, 8–20. [CrossRef]

7.　Hooper, A.; Zebker, H.; Segall, P.; Kampes, B. A new method for measuring deformation on volcanoes and other natural terrains using InSAR persistent scatterers. *Geophys. Res. Lett.* **2004**, *31*, 275–295. [CrossRef]

8.　Berardino, P.; Fornaro, G.; Lanari, R.; Sansosti, E. A new algorithm for surface deformation monitoring based on small baseline differential interferograms. *IEEE Trans. Geosci. Remote Sens.* **2002**, *40*, 2375–2383. [CrossRef]

9.　Lu, Z.; Dzurisin, D.; Biggs, J.; Wicks, C., Jr.; McNutt, S. Ground surface deformation patterns, magma supply, and magma storage at Okmok volcano, Alaska, from InSAR analysis: 1. Intereruption deformation, 1997–2008. *J. Geophys. Res.* **2010**, *115*, B00B02. [CrossRef]

10.　Papoutsis, I.; Kontoes, C.; Massinas, B.; Paradissis, D.; Frangos, P. Assessing pre-seismic and post-seismic displacement in the Athens metropolitan area by SAR interferometric point target analysis, using ERS and ENVISAT datasets. In Proceedings of the Advances in the Science and Applications of SAR Interferometry ESA ESRIN, Frascati, Italy, 30 November–4 December 2009.

11.　Farinaa, P.; Colombob, D.; Fumagallib, A.; Marks, F.; Moretti, S. Permanent scatterers for landslide investigations: Outcomes from the ESA-SLAM project. *Eng. Geol.* **2006**, *88*, 200–217. [CrossRef]

12.　Liu, P.; Li, Z.; Hoey, T.; Kincal, C.; Zhang, J.; Muller, J.-P. Using advanced InSAR time series techniques to monitor landslide movements in Badong of the three gorges region, China. *Int. J. Appl. Earth Observ. Geoinform.* **2013**, *21*, 253–264. [CrossRef]

13.　Bouali, E.H.; Thomas, O.; Rüdiger, E. Interferometric stacking toward geohazard identification and geotechnical asset monitoring. *J. Infrastruct. Syst.* **2016**. [CrossRef]

14.　Adam, N.; Parizzi, A.; Eineder, M.; Crosetto, M. Practical persistent scatterer processing validation in the course of the terrafirma project. *J. Appl. Geophys.* **2009**, *69*, 59–65. [CrossRef]

15.　Gong, H.L.; Zhang, Y.Q.; Li, X.J.; Lu, X.J.; Chen, B.B.; Gu, Z.Q. Research on the land subsidence of Beijing based on PS-InSAR technology. *Prog. Natl. Sci.* **2009**, *19*, 1261–1266. (In Chinese)

16.　Chen, B.B.; Gong, H.L.; Li, X.J.; Zhang, Y.Q.; Dang, Y.N.; Song, L.L. Monitoring and risk analysis of land subsidence in Beijing based on interferometric synthetic aperture radar (InSAR) technique. *Geogr. Geo-Inform. Sci.* **2011**, *27*, 16–20. (In Chinese)

17.　Hu, B.; Wang, H.S.; Sun, Y.L.; Hou, J.G.; Liang, J. Long-Term land subsidence monitoring of Beijing (China) using the small baseline subset (SBAS) technique. *Remote Sens.* **2014**, *6*, 3648–3661. [CrossRef]

18.　Fan, J.H.; Guo, H.D.; Guo, X.F.; Liu, G.; Ge, D.Q.; Liu, S.W. Monitoring subsidence in Tianjin area using interferogram stacking based on coherent targets. *J. Remote Sens.* **2008**, *12*, 111–118. (In Chinese)

19.　Liu, G.X.; Jia, H.G.; Nie, Y.J.; Li, T.; Zhang, R.; Yu, B. detecting subsidence in coastal areas by ultrashort-baseline TCPInSAR on the time series of high-resolution TerraSAR-X images. *IEEE Trans. Geosci. Remote Sens.* **2014**, *52*, 1911–1923.

20.　Luo, Q.; Perissin, D.; Lin, H.; Zhang, Y.; Wang, W. Subsidence monitoring of Tianjin suburbs by TerraSAR-X persistent scatterers interferometry. *IEEE J. Sel. Top. Appl. Earth Observ. Remote Sens.* **2014**, *7*, 1642–1650. [CrossRef]

21.　Ge, D.Q.; Wang, Y.; Guo, X.F.; Fan, J.H.; Liu, S.W. Surface deformation field monitoring by use of small-baseline differential interferograms stack. *J. Geod. Geodyn.* **2008**, *28*, 61–66.

22.　Ge, D.Q.; Wang, Y.; Guo, X.F.; Liu, S.W.; Fan, J.H. Surface deformation monitoring with multi-baseline D-InSAR based on coherent point target. *J. Remote Sens.* **2007**, *11*, 574–580.

23.　Mora, O.; Mallorqui, J.J.; Broquetas, A. Linear and nonlinear terrain deformation maps from a reduced set of interferometric SAR images. *IEEE Trans. Geosci. Remote Sens.* **2003**, *41*, 2243–2253. [CrossRef]

24.　Costantini, M.; Falco, S.; Malvarosa, F.; Minati, F. A new method for identification and analysis of persistent scatterers in series of SAR images. In Proceedings of the 2008 IEEE International Geoscience and Remote Sensing Symposium, Boston, MA, USA, 7–11 July 2008.

25. Liu, G.X.; Luo, X.J.; Chen, Q.; Huang, D.F.; Ding, X.L. Detecting land subsidence in Shanghai by PS-networking SAR interferometry. *Sensors* **2008**, *8*, 4725–4741. [CrossRef]

26. Zhang, L.; Ding, X.L.; Lu, Z. Ground settlement monitoring based on temporarily coherent points between two SAR acquisitions. *ISPRS J. Photogramm.* **2011**, *66*, 146–152. [CrossRef]

27. Zhang, Y.H.; Zhang, J.X.; Wu, H.A.; Lu, Z.; Sun, G.T. Monitoring of urban subsidence with SAR interferometric point target analysis: A case study in Suzhou, China. *Int. J. Appl. Earth Observ. Geoinform.* **2011**, *13*, 812–818. [CrossRef]

28. Leijen, F.J.; Hassen, R.F. Persistent scatter interferometry using adaptive deformation models. In Proceedings of the Envisat Symposium 2007, Montreux, Switzerland, 23–27 April 2007.